

## 2 Benchmarking Machine Learning Techniques with 3 Di-Higgs Production at the LHC

---

4 B. Tannenwald<sup>a</sup> C. Neu,<sup>a</sup> A. Li,<sup>a</sup> G. Buehlmann,<sup>a</sup> A. Cuddeback,<sup>a</sup> L. Hatfield,<sup>a</sup> R.  
5 Parvatam,<sup>a</sup> C. Thompson<sup>a</sup>

6 <sup>a</sup> *University of Virginia, 248 McCormick Road, Charlottesville, VA, USA*

7 *E-mail:* [benjamin.tannenwald@cern.ch](mailto:benjamin.tannenwald@cern.ch)

8 ABSTRACT: Many domains of high energy physics analysis are starting to explore machine  
9 learning techniques. Powerful methods can be used to identify and measure rare processes  
10 from previously insurmountable backgrounds. One of the most profound Standard Model  
11 signatures still to be discovered at the LHC is the pair production of Higgs bosons through  
12 the Higgs self-coupling. The small cross section of this process makes detection very difficult  
13 even for the decay channel with the largest branching fraction ( $hh \rightarrow b\bar{b}b\bar{b}$ ). This paper  
14 benchmarks a variety of approaches (boosted decision trees, various neural network archi-  
15 tectures, semi-supervised algorithms) against one another to catalog a few of the various  
16 techniques available to high energy physicists as the era of the HL-LHC approaches.

---

## 17 Contents

18	<b>1 Introduction</b>	<b>1</b>
19	<b>2 Di-Higgs Physics</b>	<b>2</b>
20	2.1 Higgs Pair Production	2
21	2.2 Event Reconstruction	3
22	<b>3 Supervised Learning</b>	<b>6</b>
23	3.1 Boosted Decision Tree	6
24	3.2 Random Forest	7
25	3.3 Feed Forward Neural Network	8
26	3.4 Convolutional Neural Network	10
27	3.5 Energy Flow Network	13
28	<b>4 Semi-Supervised Learning</b>	<b>15</b>
29	4.1 $k$ -Means Clustering	15
30	4.2 Autoencoder	16
31	<b>5 Results</b>	<b>18</b>
32	<b>6 Conclusions</b>	<b>19</b>

---

## 33 1 Introduction

34 The use of machine learning (ML) techniques in high energy particle physics has rapidly  
35 expanded in the last few decades. The proliferation of methods and applications has touched  
36 nearly every segment of analysis and reconstruction [3] and will be vital in understanding  
37 the full dataset of the Large Hadron Collider (LHC) and data from future colliders.

38 Common approaches involve using linear techniques like decision trees and non-linear  
39 approaches like neural networks. These techniques are then used to reconstruct objects like  
40 leptons and jets, to tag b-quarks and boosted decays, and to classify different processes.  
41 Many models depend on kinematic input features physicists have traditionally used; other  
42 architectures rely on emergent features produced in a more abstract phase-space. With  
43 so many usable machine-learning options available, interesting questions arise about what  
44 types of information are best to feed to our networks. The information that is best for  
45 physicists to learn from might not be optimal for sophisticated computing algorithms.

46 The goal of this paper is to explore a wide range of current ML techniques that can be  
47 used to identify di-Higgs production at the High Luminosity LHC (HL-LHC). Observing  
48 di-Higgs production is necessary to measure the self-coupling of the Higgs boson and fully  
49 understand the nature of electroweak symmetry breaking. The difficulty in measuring

Higgs pair production lies in the tiny cross-section of even the largest branching fraction ( $hh \rightarrow b\bar{b}b\bar{b}$ ) and the relative abundance of similarly reconstructed QCD events.

This paper is organized as follows: Section 2 deals with the physics relevant for di-Higgs production and the QCD background. Sections 3 and 4 summarize the various ML methods tested. The maximum significance

$$\sigma = \frac{N_{\text{signal}}}{\sqrt{N_{\text{background}}}} \quad (1.1)$$

is provided for each method along with event yields normalized to the HL-LHC design integrated luminosity of  $3000 \text{ fb}^{-1}$ . Section 5 compares the results from the various approaches.

## 2 Di-Higgs Physics

### 2.1 Higgs Pair Production

The Higgs boson is an essential part of the Standard Model (SM) of particle physics and is a product of the mechanism responsible for electroweak symmetry breaking. Along with the interactions of the Higgs boson to the other SM particles, an additional Higgs self-coupling interaction is predicted at tree-level by the SM. This mechanism contributes to non-resonant Higgs boson pair production together with quark-loop contributions via Yukawa-type interactions. Figure 1 shows the two leading order diagrams of non-resonant Higgs boson pair production. Since the production cross section for Higgs boson pair production is extremely small within the SM [4],

$$\sigma_{hh} (14 \text{ TeV}) = 45.1 \text{ fb},$$

any significant deviation would indicate the presence of new physics.

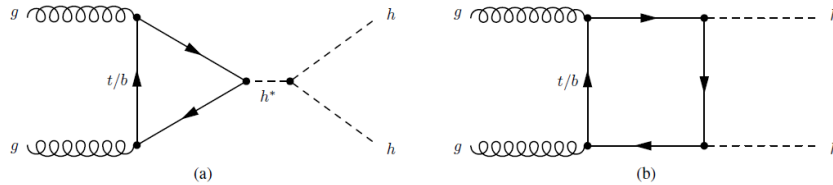


**Figure 1.** Leading order Feynman diagrams for non-resonant production of Higgs boson pairs in the Standard Model through (a) the Higgs boson self-coupling and (b) the Higgs-fermion Yukawa interaction.

Many extensions of the SM predict the existence of additional scalar bosons which may have mass larger than twice the Higgs mass and can decay into a Higgs boson pair. Searching for resonances in the  $hh$  mass spectrum can help us discover or limit exotic models which predict the presence of such particles. More importantly, measuring the SM di-Higgs cross-section (or placing limits on its magnitude) allows us to probe the self-coupling of the Higgs field and better understand the mechanism behind electroweak symmetry breaking.

The following work is focused on techniques for distinguishing non-resonant (SM-like) Higgs boson pair production where both Higgs bosons decay via  $h \rightarrow b\bar{b}$ . Using the  $4b$  decay mode provides the largest possible amount of signal events but requires powerful background reduction techniques due to the large production cross-section of fully hadronic QCD processes. All results are quoted for simulated events produced by  $pp$  collisions with a center-of-mass energy of 14 TeV and scaled to the HL-LHC design integrated luminosity of  $3000 \text{ fb}^{-1}$ . Simulated samples were produced using Madgraph v2.7.0 [6] in a ROOT v6.12/04 [5] environment. Events were then showered using Pythia v8.2.44 [7] and reconstructed with Delphes v3.0 [8] using the v2 approximation of the upgraded Phase-II CMS detector.

Both the signal and background samples were generated with minimal pileup addition sampled from a Poisson distribution with an expectation value of zero additional vertices. An additional generator-level cut requiring total hadronic energy greater than 300 GeV was applied when generating background QCD events. All code used to set up the generation environment and produce events is publicly available [9]. A summary of the sample generation details is shown in Table 1. The effective cross-sections in Table 1 are used for all event yield calculations in subsequent sections.

Name	Process	$\sigma_{\text{eff}}$ [fb]	$N_{\text{events}}$
Di-Higgs	$pp \rightarrow hh, h \rightarrow b\bar{b}$	12.4	$1 \cdot 10^6$
QCD	$pp \rightarrow b\bar{b}b\bar{b}$	441866.0	$4 \cdot 10^6$

**Table 1.** Madgraph processes, effective cross-sections, and number of generated events for the signal and background samples used in this paper. The effective cross-sections differ from the total theoretical cross-sections due to branching fractions and generation-level cuts on hadronic activity.

The assumption of zero additional background interactions per event is an unrealistic approximation of the HL-LHC environment where an average of two hundred additional pileup interactions is expected for each collision. This paper is an initial study aimed at gauging the power of various techniques in a simplified environment. Future studies will extend the approaches explored here to a realistic HL-LHC regime.

## 2.2 Event Reconstruction

The first step in reconstructing the  $4b$  system is to reconstruct and select b-jet candidates. Jets are clustered using an anti- $k_T$  algorithm with a radius of  $R=0.4$ . To be selected for use in event reconstruction, a jet must have  $p_T > 20 \text{ GeV}$  and  $|\eta| < 2.5$ . Delphes uses an internal  $b$ -tagging efficiency parameterization to predict whether jets are tagged. An event is only fully reconstructed if at least 4 jets are  $b$ -tagged (unless otherwise specified). The properties and kinematics of selected jets are shown in Figure 2. This strict requirement of having at least 4  $b$ -tags in an event helps to reduce contributions from QCD and resolve some of the combinatoric ambiguity in event reconstruction.

Once events with at least 4  $b$ -tags are selected, there is a choice about how to reconstruct the di-Higgs system. Several reconstruction methods were tested for pairing b-jets to find an optimal algorithm for correctly pairing Higgs boson constituents. Two algorithms were

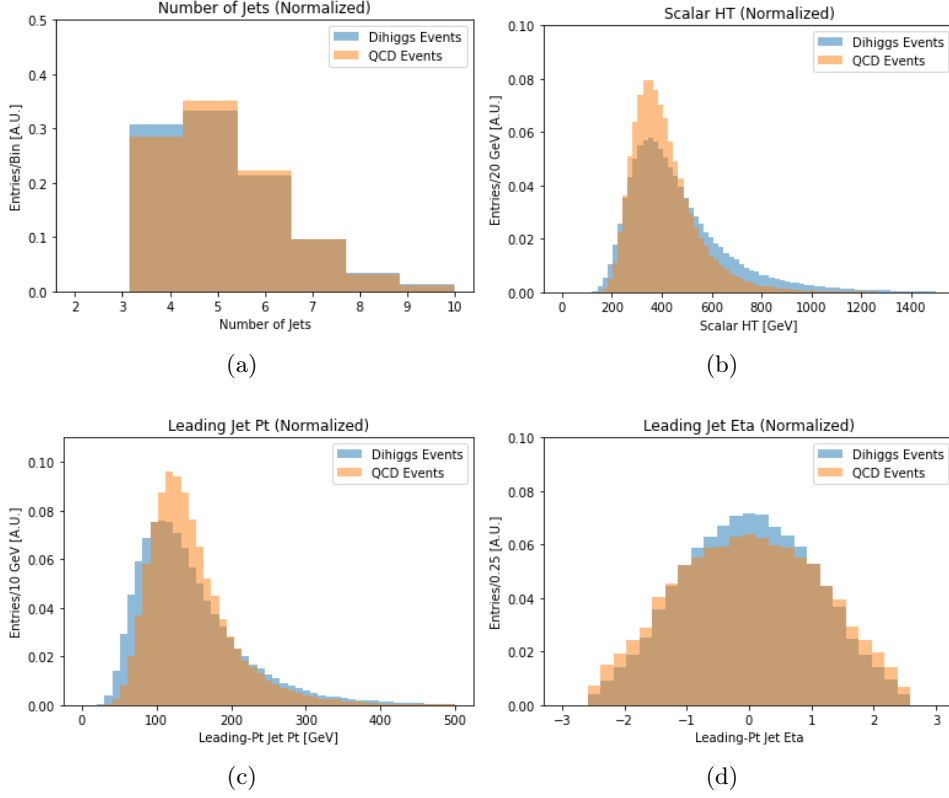


**Figure 2.** Sample of event information and leading jet kinematics from QCD and di-Higgs simulation. Distributions are normalized to the same area to compare shapes.

109 selected for use in the following sections: the first iterates through all selected jets in an  
 110 event and returns the two pairs with closest di-jet masses to one another. The second  
 111 returns the two jet pairs that yield two Higgs candidates with masses closest to the known  
 112 Higgs boson mass by minimizing the quantity

$$\chi^2 = \left( \frac{m_1 - m_h}{\sigma_h} \right)^2 + \left( \frac{m_2 - m_h}{\sigma_h} \right)^2$$

113 where  $m_{1,2}$  are the candidate di-jet masses,  $m_h = 125$  GeV is Higgs boson mass, and  $\sigma_h = 10$   
 114 GeV is the expected experimental resolution of the Higgs boson in the  $b\bar{b}$  decay channel.  
 115 Unless otherwise specified, the method that selects di-jets with masses closest to each other  
 116 is used when training algorithms that require reconstructed events. Fig 3 shows a selection  
 117 of distributions describing the di-Higgs system using this reconstruction algorithm.

118 Reconstructed variables include the masses and momentum of the two- and four-body  
 119 Higgs candidates as well as the angular separations between the two Higgs candidates and  
 120 their constituent jets. Additional event-level variables like the number of selected jets, the  
 121 number of b-tagged jets, and the missing transverse energy in the event were also considered  
 122 as inputs to various algorithms. A full list of all variables considered for each approach is  
 123 given in Table 2. All variables were evaluated using the Kolmogorov-Smirnov (KS) test for

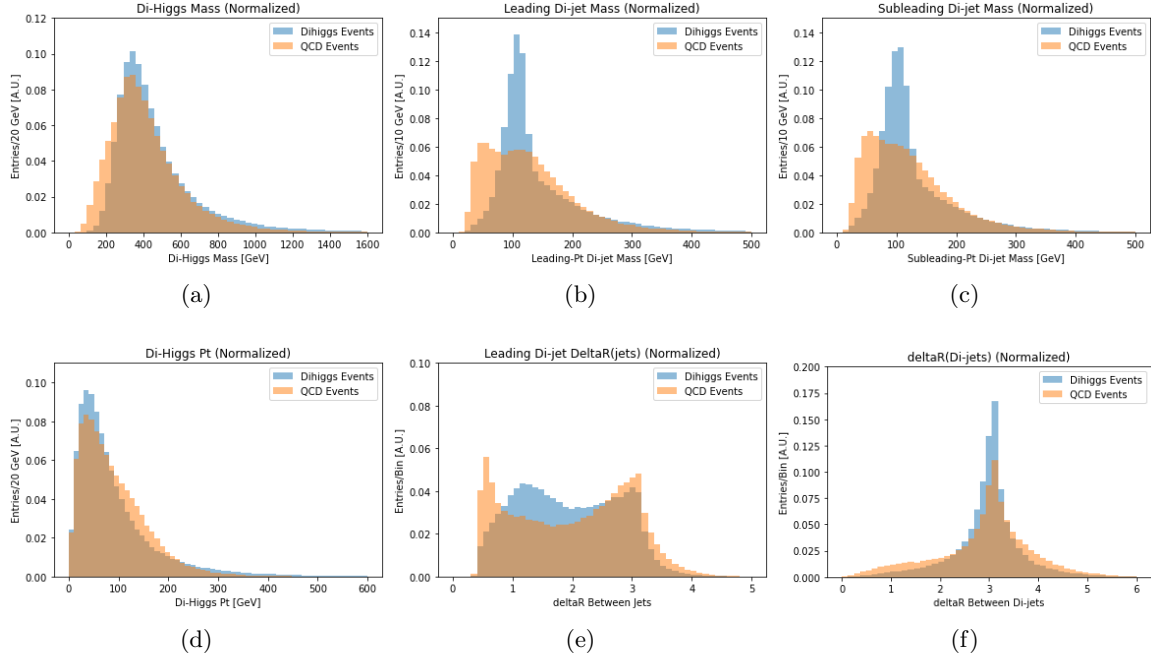


**Figure 3.** Sample of reconstructed kinematics of the di-Higgs system in QCD and di-Higgs simulation. Distributions are normalized to the same area to compare shapes.

individual separation power between signal and background. Variables were then sorted in descending order of KS separability. Each algorithm is trained on a subset that minimizes the number of variables while not sacrificing performance.

Event-Level	Reconstructed		
	di-Higgs System	Higgs Candidates	Jet Variables
$N_{\text{jets}}, N_{\text{b-tags}}$ Missing $E_T$ , Scalar $H_T$	$m_{hh}, p_T^{hh}, \eta^{hh}, \phi^{hh},$ $\Delta R(h1, h2),$ $\Delta \phi(h1, h2)$	$m_{h1}, p_T^{h1}, \eta^{h1}, \phi^{h1},$ $m_{h2}, p_T^{h2}, \eta^{h2}, \phi^{h2},$ $\Delta R(h1 \text{ jets}), \Delta R(h2 \text{ jets}),$ $\Delta \phi(h1 \text{ jets}), \Delta \phi(h2 \text{ jets})$	$p_{Tj}^{(i=1-4)}, \eta_{Tj}^{(i=1-4)}, \phi_{Tj}^{(i=1-4)},$ $\text{b-tag}^{(i=1-4)}$

**Table 2.** Complete list of all variables considered for analysis in each method. Event-level variables require no di-Higgs reconstruction. Reconstructed variables are defined only after selecting the jet pairs to reconstruct the di-Higgs system in each event. The sub/superscript 'hh' corresponds to the four-body di-Higgs system, the sub/superscript 'h1' corresponds to the leading  $p_T$  Higgs candidate, and the sub/superscript 'h2' corresponds to the sub-leading  $p_T$  Higgs candidate. Kinematic for all individual jets chosen by the reconstruction are also available for use in training classification algorithms.

## 3 Supervised Learning

Searches for specific signatures or interactions in collider data can be thought of as a classification problem - some known signal process must be identified and separated from some known and well-modeled set of background processes. Any iterative algorithm can then improve its ability to properly identify signal from background by comparing its predicted classifications to the true known classifications and adjusting its internal parameters. This type of approach is known as supervised machine learning, and it is particularly relevant when training models to distinguish between different known processes. We discuss several supervised learning approaches below.

### 3.1 Boosted Decision Tree

Boosted Decision Trees (BDTs) have a long history in high energy physics from enabling the first observation of single top production at the Tevatron [1, 2] to helping in the discovery of the Higgs boson at the LHC [10, 11]. A decision tree functions by making a series of sequential cuts (or decisions) that each maximize the separation between signal and background events for a single variable. This separation is maximized by calculating the Gini impurity index

$$I = 1 - \sum_{i=1}^J p_i^2$$

where  $i$  runs over the number of classes in a dataset and  $p_i$  is the fraction of items labeled as class  $i$  in the set after a tree split. By maximizing the purity produced by subsequent cuts, a well-designed decision tree efficiently splits the original dataset into independent sub-populations grouped by class.

Any series of cuts for identifying events will inevitably misclassify some events, and there are many strategies for improving the results. A boosted decision tree attempts to improve the classification by creating a new set of data from the improperly classified events and training a new decision tree on these inputs. Each step of re-training with misclassified events is called a *boost*, and the total prediction for an event is the weighted sum of predictions from the original tree plus the predictions from the boosted trees where each sequential boost receives a smaller weight in the sum.

The BDT trained for di-Higgs detection was built using the xgboost package [12]. The top seventeen reconstructed and event-level variables ranked by KS separability (see Table 2 for a summary of variables) were used in training. These included the mass, momentum, and angular separation variables for the di-Higgs system and the Higgs candidate di-jets. Event-level variables (e.g.  $N_{\text{b-tags}}$ ,  $N_{\text{jets}}$ ) and individual jet momenta were also used in training.

A set of tuneable variables called hyperparameters determine the training behavior and ultimate performance of any machine learning model include BDTs. Of all the hyperparameters that describe the BDT, five were found to have significant impact on the final performance of the model: the multiplicative boost factor described above, the maximum number of decisions allowed per tree (max depth), a minimum separation improvement

159 necessary for a further cut ( $\gamma$ ), a term that reduces large absolute boosted corrections  
 160 (L1 regularization or  $\alpha$ ), and a term that reduces the impact of large squared corrections  
 161 in each boost (L2 regularization or  $\lambda$ ). Regularization terms are a common element of  
 162 many machine learning algorithms and are helpful in avoiding in over-training. The set of  
 163 hyperparameters that yielded the best significance for the BDT were found to be: boost  
 164 factor of 0.1, maximum tree depth of 9,  $\gamma$  of 1.1, L1 regularization term of 22.1, and an L2  
 165 regularization term of 8.3.

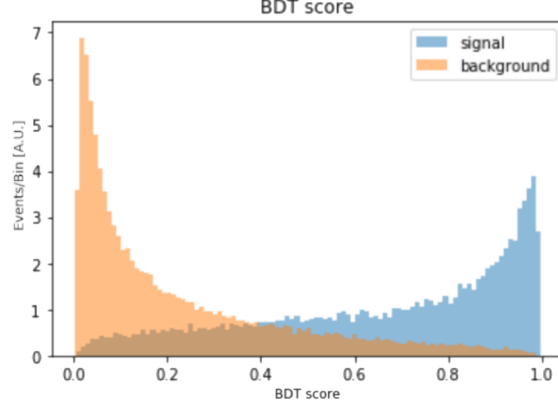


**Figure 4.** Signal predictions of the trained BDT for independent signal and background samples not used for training.

166 The predictions from the optimized BDT are shown in Figure 4. A maximum sig-  
 167 nificance of  $1.84 \pm 0.09$  was obtained, yielding  $986.3 \pm 8.9$  signal events and  $2.8 \pm 0.1 \cdot 10^5$   
 168 background events.

### 169 **3.2 Random Forest**

170 Random Forest algorithms share a similar tree structure with BDTs, but they leverage  
 171 ensembles of independent decision trees as opposed to iteratively improving the predictions  
 172 of a single tree using misclassified events. Each tree in a random forest is ‘grown’ using a  
 173 random sampling of input variables and training events. The randomness of the sampling  
 174 ensures each tree yields a unique but correlated prediction compared to the other trees in  
 175 the forest. The class prediction of the forest is the majority vote of the constituent trees.  
 176 Tuning the hyperparameters of a random forest requires optimizing the number of trees  
 177 in the forest, the variable sub-sampling used to produce each tree, and the depth of the  
 178 constituent trees.

179 The random forest trained for di-Higgs classification uses the reconstruction algorithm  
 180 that selects di-jet pairs consistent with a Higgs mass hypothesis, and the same reconstructed  
 181 and event-level variables used for the BDT were used as input to the forest. The random  
 182 forest was implemented using xgboost [12]. Five hyperparameters were found to have a  
 183 meaningful impact on the performance of the model: the number of trees in the forest,  
 184 the maximum tree depth, a L1 regularization term, the fraction of events used as inputs



to each tree (sub-sample fraction), and the fraction of reconstruction variables randomly selected as inputs for each tree (the column sub-sampling rate). Similar to the approach for optimizing the hyperparameters of the BDT, an optimal random forest configuration was obtained by individually varying each significant hyperparameter over a reasonable range and selecting the best performing model.

The optimal random forest was training with 300 constituent trees, a maximum tree depth of 20, a L1 regularization term of 1.175, a sub-sampling fraction of 0.8, and a column sub-sampling rate of 0.8,. The best significance for the random forest approach was found to be  $\sigma = 2.44 \pm 0.19$  when requiring a prediction score  $> 0.80$ . This region yielded an expectation of  $544.7 \pm 6.3$  signal events and  $5.0 \pm 0.5 \cdot 10^4$  background events. Distributions of the predictions for signal and background are shown in Figure 5.

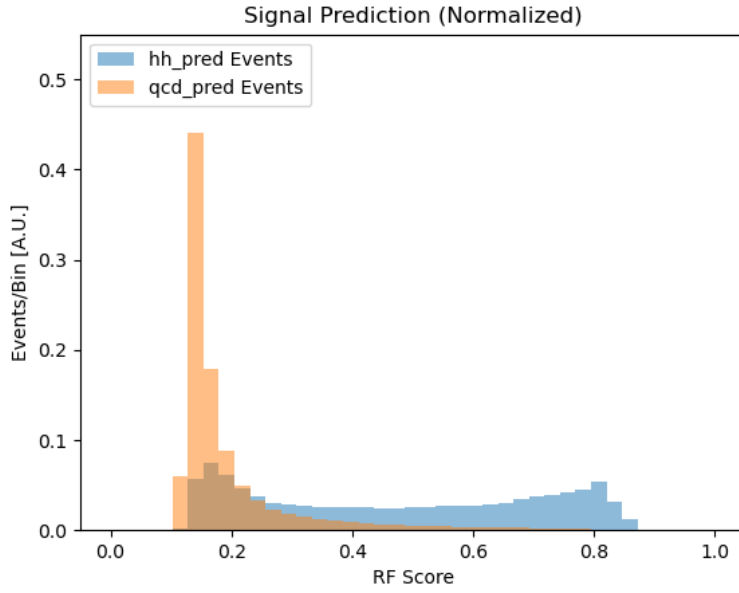


**Figure 5.** Output score on the testing dataset with the fully trained random forest classifier.

### 3.3 Feed Forward Neural Network

Fully connected or feed-forward neural networks (NNs) also have a long history in high energy physics. The fundamental element of any neural network is called a *layer*. Multiple layers are stacked together to produce a final prediction given the input variables from the first layer. This predicted outcome is then evaluated against a known target value. A fully-connected network can have multiple internal (or hidden) layers between the input and output layers, and each hidden layer is composed of a series of trainable activation functions and weights that allow the network to identify and iteratively combine important features of the input space. A function (called the loss function) is chosen to quantify the difference between the model prediction and target values. The loss calculated after a

single training iteration is used to adjust the internal network weights in the next training iteration through a process called backpropagation. The model is fully trained once the improvement in the loss between iterations falls beneath some user-defined threshold.

The NN trained for di-Higgs detection was built using the Keras [13] and Tensorflow [14] packages. The top twenty-two most separable reconstructed and event-level variables were used as the input variables for the NN. These included the mass, momentum, and angular separation variables for the di-Higgs system and the Higgs candidate di-jets, momentum and angular information from the individual selected jets, and all event-level variables. Hyperparameter optimization for neural networks involves the additional step of designing the structure of the network: how many hidden layers to use, how many nodes per hidden layer, dropout layers which remove random weights in each training iteration to prevent over-fitting, batch normalization layers which reduce the impact of very large neuron weights. Several models were trained by individually tuning each hyperparameter over a reasonable range in order to produce a final optimized model. The number of hidden layers was similarly optimized by training models with one, two, three, and four hidden layers. No networks with more than four hidden layers were tested in order to keep the number of trainable model parameters below approximately one tenth the number of training events.

The final network structure consisted of the input layer, two hidden layers, and a single-node output layer. The first hidden layer contained 175 nodes with an L2 kernel regularizer ( $\lambda = 10^{-4}$ ). The second hidden layer contained 90 nodes with no kernel regularizer. A batch normalization layer and a dropout layer (dropout fraction 0.2) were placed in between the two hidden layers to prevent over-fitting. Both hidden layers used a rectified linear (ReLU) activation function, while the output layer used a sigmoid activation function. The final performance was found to be independent of the choice of activation functions, and they are included here for completeness. The binary cross-entropy loss function

$$L = -(y \log(p) + (1 - y) \log(1 - p))$$

was used for the backpropagation. Here  $y$  represents the known binary target classifications,  $p$  represents the predicted probabilities that a given event is signal or background, and  $\log$  is the natural logarithm. A schematic flowchart of the network structure is shown in Figure 6.

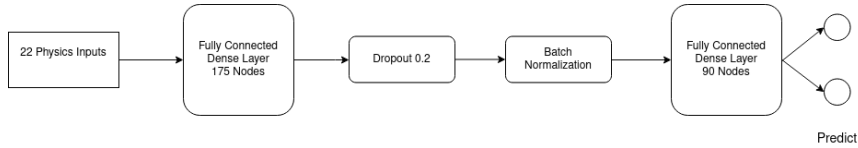


**Figure 6.** Structure of the feed-forward neural network. The input variables are fed through two fully connected dense layers to classify events. One dropout layer and one batch normalization layer help mitigate over-fitting during training.

The NN was trained for 25 epochs before the minimal loss-improvement threshold was met, and the results are shown in Figure 7. The trained model obtained a maximum  $\sigma = 2.40 \pm 0.08$  when considering events with a signal prediction score  $> 0.94$ . This phase-space has a signal yield of  $1659.9 \pm 12.5$  events and a background yield of  $4.8 \pm 0.2 \cdot 10^5$  events.

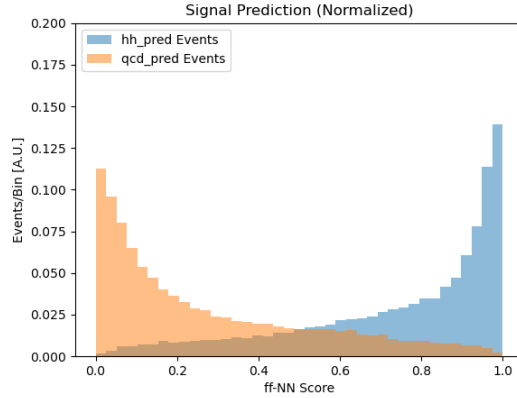


**Figure 7.** Final predictions of the feed-forward network for signal and background samples.

### 230 3.4 Convolutional Neural Network

231 Convolutional Neural Networks (CNNs) are neural networks that predict the content of an  
 232 input image by using assumptions about the local relationships between neighboring pixels.  
 233 For this analysis, content prediction is simplified to a general classification of whether the  
 234 image comes from a di-Higgs or QCD event. The fundamental elements of any convolutional  
 235 network are convolutional layers and pooling layers. Convolutional layers use filters that  
 236 perform linear combinations of neighboring pixels within the filter size, and pooling layers  
 237 aggregate information by grouping neighboring pixels using either their maximum or average  
 238 values. After some number of these layers, the output is flattened into a one-dimensional  
 239 vector, and this flattened vector is pushed through a set of feed-forward layers in order to  
 240 make a final output prediction.

241 Many previous papers have explored the use of convolutional networks trained on low-  
 242 level quantities (e.g. tracks and calorimeter deposits) for the purposes of object identifica-  
 243 tion [15] at colliders. This paper extends the application to event-level identification. Using  
 244 low-level quantities removes the need to reconstruct higher-level objects like jets or jet pairs;  
 245 only the detector-level measurements are required for image creation. The performance of  
 246 four convolutional networks was studied in the context of di-Higgs identification. The first  
 247 network used a 3-layer image composed of energy/momentum weighted tracks, electromag-  
 248 netic calorimeter deposits, and hadronic calorimeter deposits. The second network used the  
 249 same three layers but appended additional global event-level information to the flattened  
 250 vector after image processing and before the fully connected layers. Figures 8 and 9 depict  
 251 both network structures. The third and fourth networks followed the same pattern as the  
 252 previous two but with the addition of two image layers corresponding to longitudinal and  
 253 transverse impact parameter-weighted track information.

254 In order to produce coherent images, the center of mass and the center of momentum  
 255 for each event are calculated. All constituents are then boosted longitudinally into the  
 256 center of mass of the event and rotated in phi to the center of momentum. After this pre-

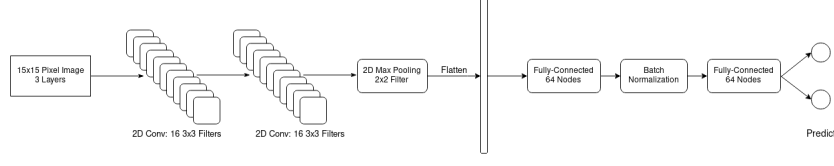


**Figure 8.** Structure of the nominal convolutional neural network. The input images are fed through two convolutional layers and a single max-pooling layer before being flattened into a one-dimensional vector. The flattened vector is then fed through one fully connected layer, a batch normalization layer, and a final fully connected layer before a final prediction is made.

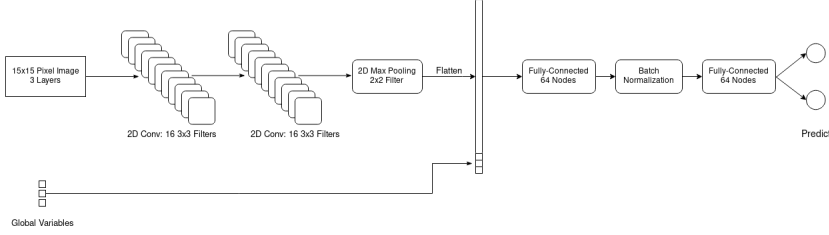


**Figure 9.** Structure of the hybrid convolutional neural network. The input images are fed through two convolutional layers and a single max-pooling layer before being flattened into a one-dimensional vector. Scaled user-specified variables (e.g.  $H_T$ ) are then concatenated with the flattened image vector. The concatenated vector is then fed through one fully connected layer, a batch normalization layer, and a final fully connected layer before a final prediction is made.

processing, each image layer corresponds to a 31x31 pixel grid centered on the total activity in the event. Figure 10 shows the average di-Higgs image layers (a–e) and the average QCD image layers (f–j). While the average image layers for each sample closely resemble one another, they do contain different information, and variations are visible.

Importantly, clear differences are observed between the average QCD images and the average di-Higgs images. Each half of the di-Higgs image (split across  $\phi = 0$ ) is arranged in a roughly circular, isotropic shape due to the spin-0 nature of the Higgs. The QCD images appear balanced because of the effect of the pre-processing, but no similar circular structure is produced. Additionally, the variance of pixel intensities in di-Higgs images is much smaller than the variance in QCD images due to the more balanced kinematics of Higgs pair production compared to QCD processes.

As shown in Figures 8 and 9, the CNN network structure uses two sequential 2D convolutional layers each with 16 3x3 filters, one max-pooling layer with a 2x2 window, a flattening of the outputs, two 64-node fully connected hidden layers, and one output layer for making the final prediction. As previously described, two of the networks append additional high level variables (scalar sum of transverse hadronic energy, number of jets, and number of  $b$ -tags) after the flattening and before the image information is fed through the fully connected layers. The optimal significance for each network is shown in Table 3.

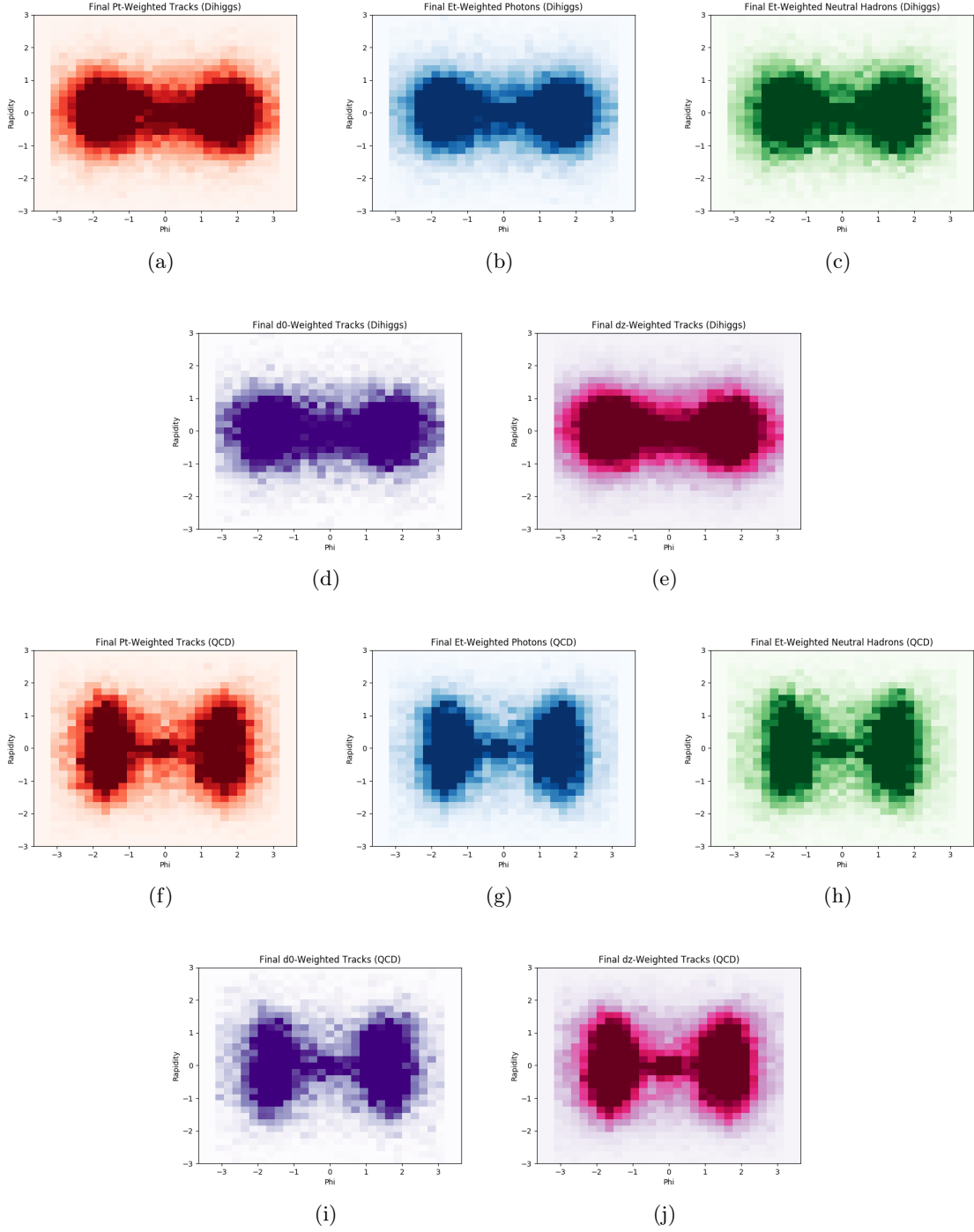


**Figure 10.** Average image layers for di-Higgs (a-e) and QCD (f-j) decays. Sub-figures (a) and (f) show  $p_T$ -weighted tracks, (b) and (g) show  $E_T$ -weighted ECAL deposits, (c) and (h) show  $E_T$ -weighted HCAL deposits, (d) and (i) show transverse impact parameter-weighted tracks, (e) and (j) show longitudinal impact parameter-weighted tracks.

275 The best results were obtained using the 5-color network with additional high-level inputs,  
 276 and the final predictions for this configuration are shown in Figure 11. A best significance  
 277 of  $2.86 \pm 0.03$  was found for a prediction cut  $> 0.94$  with a signal yield of  $1.00 \pm 0.05 \cdot 10^4$   
 278 events and a background yield of  $1.32 \pm 0.01 \cdot 10^7$  events.

Method	Best $\sigma$	AUC
Tracks+HCAL+ECAL	$1.77 \pm 0.01$	0.818
Tracks+HCAL+ECAL + high-level	$2.12 \pm 0.01$	0.846
Tracks+HCAL+ECAL+D0+DZ	$2.45 \pm 0.02$	0.863
Tracks+HCAL+ECAL+D0+DZ + high-level	$2.86 \pm 0.03$	0.882

**Table 3.** Normalized to full HL-LHC dataset of  $3000 \text{ fb}^{-1}$

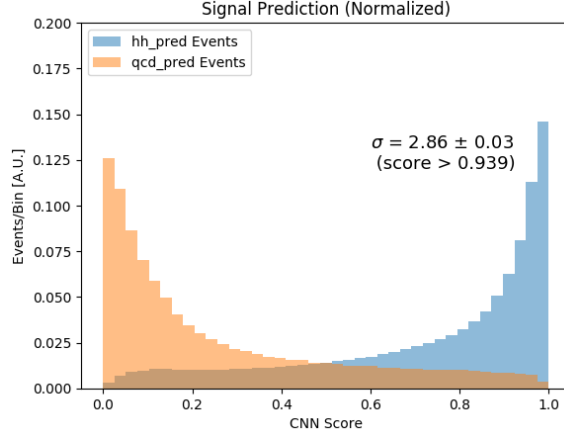


**Figure 11.** Signal prediction for the 5-color convolutional network with additional high-level inputs. The total area of the signal and background predictions are normalized to unity for easier shape comparison.

### 279 3.5 Energy Flow Network

280 Energy Flow Networks (EFN) and Particle Flow Networks (PFN) are neural networks that  
 281 also operate with basic jet constituent information as input rather than reconstructed jets  
 282 and multi-jet composites [16]. The EFN structure takes only the rapidity,  $y$ , and azimuthal  
 283 angle,  $\phi$ , of jet constituents as input, while the PFN takes the rapidity, azimuthal angle,  
 284 and transverse momentum,  $p_T$ , of jet constituents as input. Both the EFN and PFN are  
 285 two-component networks, and their internal structures are shown in Figure 12.

286 Network (a) takes jet constituent information as input and uses a set of fully connected  
 287 neural network layers to produce a set of latent features,  $\Phi$ . Linear combinations of the  
 288 latent variables,  $\mathcal{O}$  are then used as the input for network (b) which uses another set of  
 289 fully connected layers to produce final predictions. The EFN and PFN used for di-Higgs

classification use 200 nodes for each hidden layer in network (a), 256 nodes for the latent  
space dimension, and 300 nodes for each hidden layer in network (b).

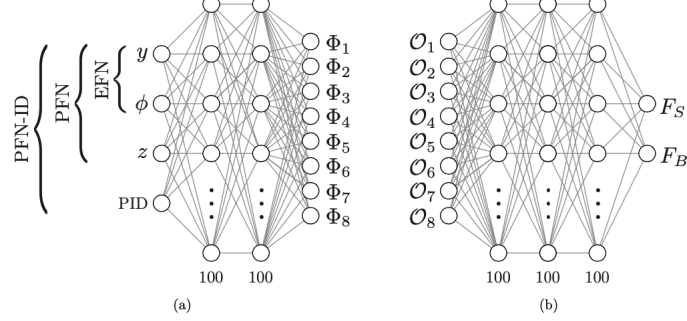


**Figure 12.** Example of a complete EFN/PFN network. Network (a) uses jet constituent information as input and outputs a set of latent variables,  $\Phi$ . Network (b) produces linear combinations,  $\mathcal{O}$ , of the latent variables which are then fed through several fully connected layers to make a final prediction.

The EFN/PFN networks were trained using four separate categories split by number of jets and number of  $b$ -tags to test the network's dependence on higher-level jet information. Independent networks were trained using: all events, only events with  $\geq 4$  jets, only events with  $\geq 4$  jets and  $=2$   $b$ -tags, and only events with  $\geq 4$  jets and  $\geq 4$   $b$ -tags. In each configuration, the number of signal and background events were adjusted to maintain an equal proportion of each population in the training sample. L2 regularization and dropout layers were added to minimize over-fitting. The results obtained from each EFN configuration are shown in Table 4. The results of each PFN configuration are shown in Table 5.

Category	0PU		
	Best $\sigma$	$N_{\text{Signal}}$	$N_{\text{Background}}$
All Events	$1.407 \pm 0.006$	$1.89 \pm 0.01 \cdot 10^4$	$1.80 \pm 0.01 \cdot 10^8$
4Jets	$1.363 \pm 0.006$	$1.63 \pm 0.01 \cdot 10^4$	$1.43 \pm 0.01 \cdot 10^8$
4Jets 2BTags	$1.343 \pm 0.006$	$1.33 \pm 0.01 \cdot 10^4$	$9.95 \pm 0.06 \cdot 10^7$
4Jets 4BTags	$0.867 \pm 0.008$	$3468.7 \pm 21.1$	$1.60 \pm 0.01 \cdot 10^7$

**Table 4.** Results of the optimal EFN performance across categories. Event yields normalized to the full HL-LHC dataset of  $3000 \text{ fb}^{-1}$ . The provided errors take into account the Monte Carlo statistical uncertainty and the uncertainty on the Madgraph generated cross-section.

Both networks performed best when trained over all events without any cuts on the number of jets or  $b$ -tags. The EFN obtained a highest significance of  $1.41 \pm 0.01$ , and the PFN obtained a highest significance of  $1.62 \pm 0.01$ .

Category	0PU		
	Best $\sigma$	$N_{\text{Signal}}$	$N_{\text{Background}}$
All Events	$1.618 \pm 0.008$	$1.79 \pm 0.01 \cdot 10^4$	$1.21 \pm 0.01 \cdot 10^8$
4Jets	$1.580 \pm 0.008$	$1.32 \pm 0.01 \cdot 10^4$	$7.00 \pm 0.04 \cdot 10^7$
4Jets 2BTags	$1.574 \pm 0.009$	$1.32 \pm 0.01 \cdot 10^4$	$4.85 \pm 0.03 \cdot 10^7$
4Jets 4BTags	$0.903 \pm 0.009$	$3297.3 \pm 20.4$	$1.33 \pm 0.01 \cdot 10^7$

**Table 5.** Results of the optimal PFN performance across categories. Event yields normalized to the full HL-LHC dataset of  $3000 \text{ fb}^{-1}$ . The provided errors take into account the Monte Carlo statistical uncertainty and the uncertainty on the Madgraph generated cross-section.

## 303 4 Semi-Supervised Learning

304 While it makes sense to treat searches for new physics or rare signatures as a supervised  
305 classification problem, an alternative approach is to let an algorithm learn intrinsic features  
306 from an unlabeled dataset and then evaluate whether this self-learned information can be  
307 used to identify sub-samples within a complete data set. The process of learning features  
308 from unlabeled datasets is called unsupervised learning. Unsupervised machine learning  
309 can be transformed into semi-supervised learning when the results of unsupervised learning  
310 are evaluated using known classification information.

### 311 4.1 $k$ -Means Clustering

312 K-means clustering is an unsupervised learning algorithm that finds natural unlabeled  
313 groupings in a scaled phase-space describing the input dataset. Scaled data is created  
314 by compressing or stretching each variable of the dataset to the same maximum and min-  
315 imum values. This ensures each variable is treated equally when calculated the distances  
316 between neighboring points. Minimum values of 0 and maximum values of 1 were chosen  
317 for all variables in this analysis.

318 The k-means approach creates clusters by randomly seeding a user-specified number of  
319 cluster centroids in the scaled phase-space. Each point is associated to the closest nearby  
320 centroid, and the group of points belonging to a single centroid is defined as a cluster. The  
321 centroid positions are updated over several iterations by minimizing the ensemble sum of  
322 the squared distance between a centroid and all points associated to that cluster. As the  
323 centroids move, points can be associated to different clusters eventually obtaining a set  
324 of clusters defined by locally dense groupings of similar points. Combining unsupervised  
325 clustering with the supervised structure of a BDT converts the unsupervised approach  
326 into a semi-supervised algorithm whose performance can be compared to other supervised  
327 methods.

328 The number of clusters,  $k$ , to fit is a user-defined hyperparameter, and the number of  
329 clusters used to describe a dataset must be carefully chosen. Using too few clusters risks  
330 not being able to identify meaningfully different populations in the input dataset. Using  
331 too many clusters risks losing predictive power by splitting coherent sets of points into  
332 arbitrary groupings. An optimal  $k$  is found by scanning several values, calculating the total



distance between all points and their associated centroid, and selecting a  $k$  that minimizes this distance without asymptotically approaching zero.

The optimal  $k$  for the di-Higgs data was found lie around 20, and three different clusterings ( $k=15, 20, 40$ ) were tested for completeness. The scenarios with 15 and 40 clusters test the effects of under-clustering and over-clustering respectively. Two sets of clustered data were used as input to the nominal BDT to test the performance of this semi-supervised approach. The first set used all reconstructed kinematic variables as the input to the  $k$ -means clustering stage before training the BDT. The second set was produced by performing a principal component analysis (PCA) decomposition on the nominal kinematic inputs before passing through the clustering step and the BDT. PCA is a technique for finding an orthogonal basis of the input data that minimizes the variance along each new axis. No transformation was found to improve the performance of the nominal configuration, and the results are shown in Table 6.

Method	$\sigma$	$N_{\text{sig}}$	$N_{\text{bkg}}$
Nominal BDT	$1.84 \pm 0.09$	$986.3 \pm 8.9$	$2.9 \pm 0.1 \cdot 10^5$
15 Clusters	$1.29 \pm 0.02$	$2100.2 \pm 14.6$	$2.7 \pm 0.1 \cdot 10^6$
15 Clusters + PCA	$1.25 \pm 0.02$	$2189.5 \pm 15.1$	$3.1 \pm 0.1 \cdot 10^6$
20 Clusters	$1.30 \pm 0.02$	$2260.6 \pm 15.4$	$3.0 \pm 0.1 \cdot 10^6$
20 Clusters + PCA	$1.27 \pm 0.03$	$1756.4 \pm 12.9$	$1.9 \pm 0.1 \cdot 10^6$
40 Clusters	$1.44 \pm 0.03$	$1704.6 \pm 12.7$	$1.4 \pm 0.1 \cdot 10^6$
40 Clusters + PCA	$1.34 \pm 0.02$	$2144.5 \pm 14.8$	$2.0 \pm 0.1 \cdot 10^6$

**Table 6.** Significance and yields showing BDT performance when using the nominal kinematic inputs, clustered kinematic inputs, and clustered inputs from a PCA decomposition. All yields are normalized to full HL-LHC dataset of  $3000 \text{ fb}^{-1}$ .

## 4.2 Autoencoder

An autoencoder (AE) is an unsupervised machine learning architecture used for detecting anomalies that differ significantly from the data used to train the network. The structure of the AE compresses the input information into a lower-dimensional representation called the latent space. This compression ‘encodes’ the most important features of the training data into the latent space, while the second half of the network ‘decodes’ the latent space back into a representation approaching the original inputs.

This construction fundamentally changes the meaning of the loss calculation— rather than computing the loss between a prediction and a target, the AE loss is a measure of how well the network reproduces the original inputs after encoding and decoding. Inputs that differ significantly from the data used to train the AE will not be properly reconstructed, and anomalies can be identified by selecting events with large losses. Training with Monte Carlo simulations allows for a semi-supervised cross-check on AE performance since the classes of training and testing samples are known in advance.

Because AE anomaly detection relies on a well-modeled understanding of background processes, the network was trained using only QCD events. Additional models were trained by substituting the pure-QCD training sample with training samples consisting of mixtures of QCD and di-Higgs events to test the stability of the method against signal contamination. No significant deterioration was observed for reasonable levels of contamination. The AE used for di-Higgs detection was built using the Keras package [13] and consists of an input layer, a single hidden layer, and an output layer. Eleven reconstructed variables (di-Higgs and di-jet Higgs candidate masses, momenta, and angular variables) were selected for use in the AE.

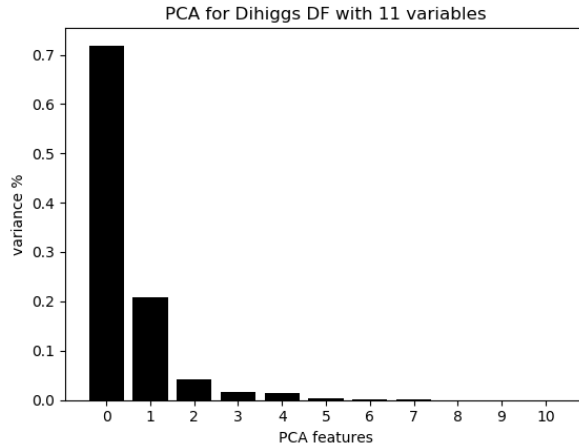


**Figure 13.** PCA performed on the selected eleven kinematic inputs. The x-axis indicates the number of PCA features, and the y-axis indicates the variance. Choosing the optimal size for the latent space requires identifying the point of diminishing variance return.

The output layer is a mirror of the input layer and therefore has 11 nodes. A PCA analysis (shown in Figure 13) was used to determine that a latent space of three nodes was optimal. Similar to the  $k$ -means clustering, the size of the latent space should be large enough to model the intrinsic features of the input data without being so large that the latent representation is able to learn features drawn arbitrarily from the input space. A PCA analysis (shown in Figure 13) was used to determine that a latent space of three nodes was able to capture over 95% of the input variance. The hidden layer and output layer use ReLU and sigmoid activation functions respectively. An L2 regularization term was added to the hidden layer to avoid over-fitting. Because training an autoencoder is an unsupervised and unlabeled process, there is no prediction of whether a given event is signal or background. Since di-Higgs events should be relatively anomalous compared to the QCD training set, signal events should have a relatively larger average loss value. Cutting on the loss function allows for a significance to be calculated for comparison with other methods.

Training for several hundred epochs leads the model to converge, and it reaches an asymptotic ensemble loss value near 0.7 (see Figure 14). A best significance of  $\sigma = 0.81 \pm 0.01$  was obtained for events with individual reconstructed loss scores greater than 0.05. The

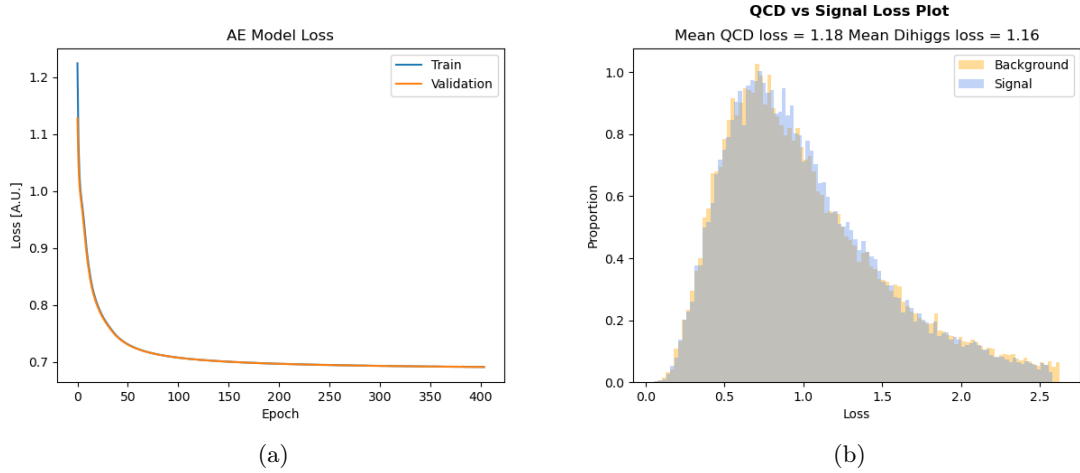


**Figure 14.** (Left) The loss of the AE during QCD training/reconstruction converged after 700 epochs. (Right) The loss distribution generated by the AE when being tested on QCD and di-Higgs event data separately.

significance obtained for lower thresholds allowed for slightly more background while the significance obtained for higher loss thresholds rejected too many signal events. Still, this optimal point is somewhat misleading since the signal and background loss distributions have little separation. The highest significance result effectively is a cut that keeps nearly all events. This suggests that the kinematic inputs used in training do not significantly differ between signal and background processes after the latent space compression.

## 5 Results

The methods covered in this paper are by no means an exhaustive review of the ML landscape available to high energy physics. Still, a wide range of techniques and philosophies are covered. Table 7 provides a summary of the methods described in the previous sections. The raw yields after selection and reconstruction cuts (depending on the method) have been weighted by the effective cross-sections listed in Table 1 and scaled to  $3000 \text{ fb}^{-1}$ . The result from a traditional 1-D sequential cut technique is shown for comparison though the details were not discussed in the previous sections. Clear gains in sensitivity compared to this baseline are apparent for many of the ML models tested in this review.

An important caveat to keep in mind is that all results discussed here were determined in conditions with zero pileup. In higher pileup environments like those expected at the HL-LHC, reconstruction algorithms see serious reductions in correct combinatoric matching. This effect will certainly degrade the expected performance of techniques that rely on explicit event reconstruction. Methods that do not rely on event reconstruction (CNN, PFN) might be more robust to these effects, and this should be studied in further work. The unsupervised AE technique performed the worst among all the methods tested, but

Method	0PU		
	Best $\sigma$	$N_{\text{Signal}}$	$N_{\text{Background}}$
Autoencoder	$0.81 \pm 0.01$	$5840.8 \pm 31.8$	$5.2 \pm 0.3 \cdot 10^7$
1D-Rectangular Cuts	$0.82 \pm 0.02$	$3621.0 \pm 21.8$	$2.0 \pm 0.2 \cdot 10^7$
k-Means Clustering	$1.44 \pm 0.02$	$1703.6 \pm 12.7$	$1.39 \pm 0.03 \cdot 10^6$
Particle Flow Network	$1.62 \pm 0.01$	$1.78 \pm 0.08 \cdot 10^4$	$1.21 \pm 0.01 \cdot 10^8$
Boosted Decision Tree	$1.84 \pm 0.09$	$986.3 \pm 8.9$	$2.8 \pm 0.1 \cdot 10^5$
Feed-Forward NN	$2.40 \pm 0.08$	$1659.9 \pm 12.9$	$4.8 \pm 0.2 \cdot 10^5$
Random Forest	$2.44 \pm 0.19$	$544.7 \pm 6.3$	$5.0 \pm 0.5 \cdot 10^4$
Convolutional NN	$2.85 \pm 0.02$	$1.00 \pm 0.05 \cdot 10^4$	$1.32 \pm 0.01 \cdot 10^7$

**Table 7.** Comparison of method significance and signal/background yields normalized to full HL-LHC dataset of  $3000 \text{ fb}^{-1}$ . The provided errors take into account the Monte Carlo statistical uncertainty and the uncertainty on the Madgraph generated cross-section.

this is likely a reflection of the fact that model-specific methods often outperform model-unspecific methods when evaluated on the model used in training.

## 6 Conclusions

Measuring the rate of di-Higgs production will be a problem facing the high energy physics community through the end of the HL-LHC era. The techniques explored in this paper show the power of machine learning techniques in identifying di-Higgs signals amid overwhelming QCD backgrounds. The significance obtained for many of these methods is impressive given the simplicity of the evaluation metric. This bodes well for both current and future measurements of Higgs pair production at the LHC.

## References

- [1] D0 collaboration, *Evidence for Production of Single Top Quarks and First Direct Measurement of  $|V_{tb}|$* , *Phys. Rev. Lett.* **98** (2007) 181802 [[hep-ex/0612052](#)].
- [2] CDF collaboration, *Measurement of the Single Top Quark Production Cross Section at CDF*, *Phys. Rev. Lett.* **101** (2008) 252001 [[0809.2581](#)].
- [3] K.A. et al., *Machine Learning in High Energy Physics Community White Paper*, 2018.
- [4] LHC HIGGS CROSS SECTION WORKING GROUP collaboration, *Handbook of LHC Higgs Cross Sections: 4. Deciphering the Nature of the Higgs Sector*, [1610.07922](#).
- [5] R. Brun and F. Rademakers, *ROOT: An Object Oriented Data Analysis Framework*, *Nucl. Instrum. Meth. A* **389** (1997) 81.
- [6] J. Alwall, R. Frederix, S. Frixione, V. Hirschi, F. Maltoni, O. Mattelaer et al., *The Automated Computation of Tree-Level and Next-to-Leading Order Differential Cross Sections, and their Matching to Parton Shower Simulations*, *JHEP* **07** (2014) 079 [[1405.0301](#)].
- [7] T. Sjöstrand, S. Ask, J.R. Christiansen, R. Corke, N. Desai, P. Ilten et al., *An Introduction to PYTHIA 8.2*, *Computer Physics Communications* **191** (2015) 159–177.
- [8] J. de Favereau, C. Delaere, P. Demin, A. Giammanco, V. Lemaître, A. Mertens et al., *DELPHES 3: A Modular Framework for Fast Simulation of a Generic Collider Experiment*, *Journal of High Energy Physics* **2014** (2014) .
- [9] B. Tannenwald, A. Li, A. Cuddeback, R. Parvatam and C. Thompson, “dihiggsMLProject.” <https://github.com/neu-physics/dihiggsMLProject>, 2020.
- [10] G. Aad, T. Abajyan, B. Abbott, J. Abdallah, S. Abdel Khalek, A. Abdelalim et al., *Observation of a New Particle in the Search for the Standard Model Higgs boson with the ATLAS detector at the LHC*, *Physics Letters B* **716** (2012) 1–29.
- [11] S. Chatrchyan, V. Khachatryan, A. Sirunyan, A. Tumasyan, W. Adam, E. Aguilo et al., *Observation of a New Boson at a Mass of 125 GeV with the CMS experiment at the LHC*, *Physics Letters B* **716** (2012) 30–61.
- [12] T. Chen and C. Guestrin, *XGBoost: A Scalable Tree Boosting System*, *CoRR* **abs/1603.02754** (2016) [[1603.02754](#)].
- [13] F. Chollet, “Keras.” <https://github.com/fchollet/keras>, 2015.
- [14] M.A. et al., *TensorFlow: Large-Scale Machine Learning on Heterogeneous Distributed Systems*, *CoRR* **abs/1603.04467** (2016) [[1603.04467](#)].
- [15] J. Alison, S. An, P. Bryant, B. Burkle, S. Gleyzer, M. Narain et al., *End-to-end Particle and Event Identification at the Large Hadron Collider with CMS Open Data*, in *Meeting of the Division of Particles and Fields of the American Physical Society*, 10, 2019 [[1910.07029](#)].
- [16] P.T. Komiske, E.M. Metodiev and J. Thaler, *Energy Flow Networks: Deep Sets for Particle Jets*, *JHEP* **01** (2019) 121 [[1810.05165](#)].